nature communications

Article

https://doi.org/10.1038/s41467-025-60241-2

Near-infrared II cyanine fluorophores with large stokes shift engineered by regulating respective absorption and emission

Received: 25 September 2024

Accepted: 20 May 2025

Diankai Liu[1,2], Zixu He[1], Wenjie Gao[1], Jizhen Shang[1,3], Yiqing Yang[1], Xiaofan Zhang[1], Xiaohua Li[1], Huimin Ma[1,2] & Wen Shi[1,2] ✉

Fluorescence bioimaging in the near-infrared II window is a promising area due to its deep tissue penetration and high contrast. However, efficient design strategies for near-infrared II fluorophores with large Stokes shifts are still scarce. Here, we develop a series of near-infrared II fluorophores (termed VIPIs) with large Stokes shifts (167-260 nm in chloroform) by conjugating *p*-aminostyryl to hemicyanines. Time dependent density functional theory calculation and transient absorption spectra reveal that the excitation process is predominantly localized within the cyanine moiety, whereas the emission process involves the charge transfer from the cyanine to styryl moiety. We demonstrate the applications of VIPIs in multicolor imaging and conjugatable modification. Finally, we show that VIPI-4 liposomes can image the fine bone structure of knee joint of female mice over 1300 nm. This work provides insights into the excited-state photophysical processes in near-infrared II window, offering inspiration for designing fluorophores with extended emission and large Stokes shifts.

Fluorescence bioimaging has revolutionized the way we observe biological processes, offering high resolution and sensitivity with minimal invasiveness[1–3]. In recent years, second near-infrared (NIR-II, 900–1700 nm) fluorescence imaging has emerged as a promising method for in vivo visualizing deeper targets with improved contrast, which also facilitates the study on the in vivo diagnosis and treatment of diseases[4–11]. This is because longer wavelength can effectively circumvent the scattering and absorption of biological tissues. As a result, the superiority of the NIR-II imaging has spurred the growing interest in the development of new NIR-II fluorophores[12–15].

Currently, derivatives of cyanine are an important category of NIR-II dyes[16–21]. These dyes have long absorption/emission wavelengths, high molar absorption coefficient, and good biocompatibility. They consist of two heterocyclic rings with a polymethine chain, and are renowned for their structural diversity. To optimize the performance of cyanine dyes for specific imaging applications, the length of the polymethine chain and the heterocyclic ring can be modified, which are two effective methods for tuning their spectral properties[22–25]. Cy11•B$(C_6F_5)_4$ and ICG-11, containing an undecmethine chain, have been synthesized and reported with a maximum absorption over 1000 nm[22,23]. In addition, more heterocycles have been proposed to replace the indole of Cy7 to develop new NIR-II dyes[25]. However, neither strategy can overcome the common flaw of the relatively small Stokes shift (about 30 nm), which can cause self-absorption and excitation leakage, leading to degraded image quality[26,27]. This is usually attributed to the symmetry of cyanine, which restricts the reorganization of exciton and leads to localized excitation (LE) and emission. Although some asymmetric cyanines have been reported to display significant advances in wavelength and quantum yield, the Stokes shift is only about 50 nm[28]. In a rare case, hemicyanines with increased asymmetry have shown improved Stokes

---

[1] Beijing National Laboratory for Molecular Sciences, Key Laboratory of Analytical Chemistry for Living Biosystems, Institute of Chemistry, Chinese Academy of Sciences, Beijing 100190, China. [2] University of Chinese Academy of Sciences, Beijing 100049, China. [3] Huzhou Key Laboratory of Medical and Environmental Applications Technologies, School of Life Sciences, Huzhou University, Huzhou, Zhejiang 313000, China. ✉ e-mail: shiwen@iccas.ac.cn

shifts up to 70 nm[29]. Obviously, effective strategies to increase the Stokes shift of cyanines are still scarce, though they would greatly promote the utility of these dyes.

In essence, Stokes shift refers to the energy difference between excitation (absorption) and emission process of fluorescence[30–36]. Larger Stokes shift is usually associated with more energy relaxing processes of the electronic excited state (S_1)[31]. Different from LE, intramolecular charge transfer (ICT) involves electron redistribution to lower energy state under excitation and is frequently adopted to construct fluorophores with bathochromic-shifted emissions. Accordingly, we envisioned that simultaneously adjusting the contributions of LE and ICT in fluorophores may improve their photophysical properties, especially Stokes shift.

In this work, we report such a study in which an asymmetric cyanine framework is engineered to achieve large Stokes shifts (167–260 nm) of NIR-II fluorophores. The fluorophores (VIPIs) are constructed by introducing *p*-aminostyryls as the electronic donor to different hemicyanine moieties. Steady state spectral analyses show that the styryl groups cause a redshift in the fluorescence emission, whereas the hemicyanine moieties mainly impact the absorption. We investigate the in-depth mechanism by transient absorption spectra and time dependent density functional theory (TD-DFT) calculation, and find that VIPIs exhibit the LE features during excitation but ICT characteristics in the emission process. Finally, we demonstrate the application of VIPIs in multicolor NIR-II bioimaging, conjugatable modification and bone imaging. In particular, VIPI-4 liposomes are successfully used to image the fine structure of knee joint in mice through the channel over 1300 nm.

Results and discussion

Design and synthesis

Similar to cyanines, xanthene dyes show small Stokes shift due to their symmetric configuration[37]. Nevertheless, in our previous work, we reported a symmetric xanthene NIR-II dye (VIX-4[38]) with unforeseen large Stokes shift (137–417 nm), indicating that *p*-aminostyryls can serve as a strong electron donor to exert the remarkable ICT effect. Inspired by this, here we incorporated *p*-aminostyryls into asymmetric hemicyanine[39] skeleton to further reinforce the ICT action. On the other hand, 1-ethyl-benzo[cd]indolium, as a better electron acceptor than indolium[40,41], was introduced to facilitate ICT as well as expand the π-conjugation. Following this design, *N,N*-dimethylstyryl (VIPI-1 and VIPI-4), julolidinestyryl (VIPI-2 and VIPI-5) and 5-(4-(*N,N*-dimethylamino)phenyl)thiophen-2-yl (VIPI-3) were coupled to the 6-position of 6-bromo-2,3-dihydro-1*H*-xanthene-4-carbaldehyde via Heck reaction and then condensed with indolium or benzoindolium via Knoevenagel reaction (Fig. 1A). Detailed syntheses and structure characterizations are provided in the Supplementary Information.

Spectroscopic properties

The absorption and fluorescence spectra of VIPIs were examined in various solvents. As depicted in Fig. S1 and Table S1, all VIPIs show the strongest fluorescence in chloroform and the fluorescence is polarity-dependent. As the polarity increases, they display bathochromic-shifted fluorescence and decreased quantum yield, consisting with the energy gap law[42]. Interestingly, in chloroform, the absorptions of VIPI-1 and VIPI-2 only slightly redshift to 715 nm and 735 nm, respectively, as compared to that (672 nm, Fig. 1B and Figure S2A) of 6-hydroxyl-hemicyanine (HHCy1); however, their emissions show significant red-

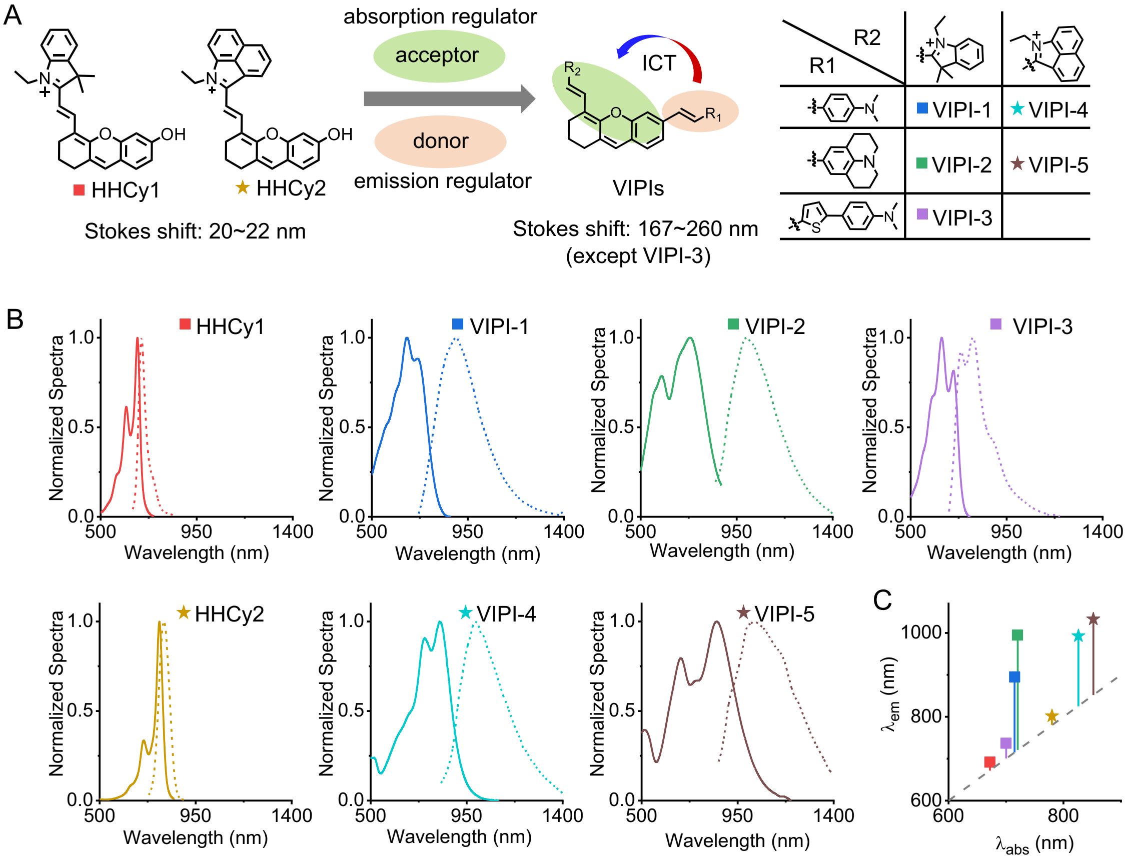

Fig. 1 | Design Scheme and Spectroscopic properties of VIPIs. A The design strategy and structures of VIPIs as well as the control cyanine dyes (HHCy1 and HHCy2). **B** Normalized absorption (solid) and fluorescence (dotted) spectra of the fluorophores in chloroform. **C** Summarized absorption (λ_{abs}) and fluorescence (λ_{em}) wavelengths of the fluorophores in panel (B). The dashed line indicates zero Stokes shift. The vertical droplines illustrate the scales of Stokes shift. The detailed spectra of VIPIs in different solvents are shown in Fig. S1.

shifts to 895 nm and 995 nm whereas the emission of HHCy1 is merely at 692 nm (Fig. 1B and Figure S2B). This remarkable difference in emission wavelength results in Stokes shifts of 180 nm and 260 nm for VIPI-1 and VIPI-2, respectively, which is far beyond those from classical cyanine dyes. In more polar solvents, the change of absorption wavelength is minimal, but the bathochromic shift of fluorescence wavelength is more pronounced, conforming to the ICT feature.

Unexpectedly, the 5-(4-(*N,N*-dimethylamino)phenyl)thiophen-2-yl group in VIPI-3 did not improve the spectroscopic property, despite its stronger electron donating ability and larger π-conjugation. VIPI-3 showed an absorption peak at 700 nm, similar to that of HHCy1, and a fluorescence spectrum with two approximate intensities at 737 nm and 790 nm, which were over 100 nm shorter than those of VIPI-1 and VIPI-2. Notably, its Stokes shift was only 37 nm, resembling that of traditional cyanines. The detailed mechanism will be discussed in the following section (*vide infra*).

For benzoindolium dyes, the absorption peaks of VIPI-4 and VIPI-5 were at 826 nm and 852 nm, respectively, which are close to that of HHCy2 at 780 nm (Fig. 1B and Fig. S2C). However, the fluorescence emissions of VIPI-4 and VIPI-5 were at 993 nm and 1033 nm, which are much longer than that of HHCy2 at 802 nm (Fig. 1B and Fig. S2D). Thus, the Stokes shifts of VIPI-4 and VIPI-5 were found to be 167 nm and 181 nm, respectively, whereas that of HHCy2 was only 22 nm. These results suggest that *p*-aminostyryl as an electron donor has a dominant impact on the emission wavelength but not absorption, which increases the Stokes shift. Interestingly, the influence of different indolium substitutions is more significant on absorption, accompanied by emission redshift (Fig. 1C).

As a common contrast agent, indocyanine green (ICG) has been used in NIR-I imaging in clinical surgical navigation[43]. Recent reports confirmed the feasibility in NIR-II imaging by using the emission tail of ICG[20,44,45]. VIPIs have similar absorption wavelengths to ICG, but their large Stokes shifts can achieve more residual fluorescence at longer wavelengths. As shown in Fig. S3A, when the solutions of VIPIs and ICG sealed in capillary tubes are imaged under different longpass (LP) filters, all of the tubes exhibit distinct fluorescence under the 1000 nm LP filter, and with the increase of cut-off wavelength, the fluorescence intensity of the tubes is decreased. If the fluorescence intensity of each tube under the 1000 nm LP filter is defined as 100%, the residual fluorescence under 1150 nm and 1300 nm LP filters can be quantified. As shown in Fig. S3B, the percentages of residual fluorescence of VIPI-3 and ICG are much lower than those of the others, and VIPI-2 displays the highest residual fluorescence under 1150 and 1300 nm LP filters. Besides, the linear relationship between the Stokes shift and the residual fluorescence of VIPIs and ICG under different LP filters can be determined (Fig. S3C), which reveals that the larger the Stokes shift of the fluorophore, the stronger its residual fluorescence in longer wavelength imaging. Therefore, using VIPIs (especially VIPI-2) in longer wavelength imaging would be helpful to improve the image quality.

Molecular calculations

The underlying mechanism for the unusually large Stokes shifts of VIPIs induced by the *p*-aminostyryl donor was explored by theoretical calculations. The density functional theory (DFT) and TD-DFT calculations were performed to obtain the optimized geometry in the ground state (S_0) and the first excited state (S_1) with the ωB97XD function and TZVP basis set. The highest occupied molecular orbital (HOMO), the second highest occupied molecular orbital (HOMO-1), and the lowest unoccupied molecular orbital (LUMO) were found to contribute mostly during the S_0-S_1 transition (Fig. S4). Interestingly, compared to HHCys, *N,N*-dimethylstyryl (VIPI-1 and VIPI-4) produced a new HOMO at about −7.0 eV, whereas julolidinestyryl (VIPI-2 and VIPI-5) generated the new HOMO at about −6.9 eV (Fig. 2). On the other hand, benzoindolium (HHCy2, VIPI-4 and VIPI-5) evidently decreased the energy level of LUMO to about −2.3 eV. These findings indicate that the *p*-aminostyryl and benzoindolium substitutions influenced the energy of the molecular orbitals separately.

To better understand the photophysical processes of VIPIs and the effect of donor-acceptor framework, we then discussed the molecular orbitals of the donor (Stys) and acceptor (HCys) separately (Fig. S5). As shown in Fig. 3A, taking VIPI-2 as an example, the LUMO of VIPI-2 is similar to that of the sub-structure HCy1 and has a high composition (85.3%; Table S3) of HCy1. This is due to the large energy difference between LUMOs of HCy1 and Sty2, making them difficult to couple. Meanwhile, the HOMO and HOMO-1 of VIPI-2 resemble the HOHOs of Sty2 and HCy1, respectively. This finding is consistent with the fact that the HOMO's energy levels of Sty2 and HCy1 are close to those of the HOMO and HOMO-1 of VIPI-2, respectively. Similar compositions can also be seen in other VIPIs (Table S3 and Figs. S6–S9).

Further, TD-DFT calculation revealed more explicit details for the excitation (absorption) and de-excitation (emission) processes between S_0 and S_1. For the control compounds of HHCys, these processes are primarily contributed by HOMO and LUMO (Figs. S10 and S11), regarded as LE. However, for VIPI-2, its excitation (S_0 to S_1) is contributed by two factors, HOMO-1 → LUMO and HOMO → LUMO (Fig. 3B). Thereinto, the HOMO-1 → LUMO transition (56.4%) even exceeds the HOMO → LUMO transition (35.7%). As discussed above, both HOMO-1 and LUMO of VIPI-2 are localized in the cyanine moiety, indicating that the excitation process of VIPI-2 contains more LE nature and primarily depends on the cyanine moiety. However, in the emission process, the contribution of the LUMO → HOMO transition (59.4%) is significantly larger than that of the LUMO → HOMO-1 transition (30.5%). From the view of charge redistribution, the LUMO → HOMO transition exhibits a stronger ICT feature than the LUMO → HOMO-1 transition. Thus, VIPI-2 has a relatively short absorption but long emission wavelength (i.e., large Stokes shift). Similar phenomena can be observed in other VIPIs except VIPI-3 (Figs. S12, S14 and S15). VIPI-3 has the largest component of LE (HOMO-1 → LUMO: 64.1%) during the excitation process (Fig. S13). Then, the LUMO → HOMO-1 transition (46.7%) still contributes more than the LUMO → HOMO transition (42.9%) in the emission process, which contains more LE component and explains the abnormal spectra of VIPI-3.

Femtosecond transient absorption spectra

The photophysical processes were further investigated by femtosecond transient absorption spectra. It is known that low-polarity solvents tend to favor the LE state, while high-polarity solvents significantly stabilize the ICT state[46]. Therefore, we analyzed the femtosecond transient absorption spectra of VIPI-2 in chloroform and DMSO as the representatives of low-polarity and high-polarity solvents.

In chloroform (Fig. 4A, B), upon excitation, the positive excited-state absorption bands of VIPI-2 appeared at 460 nm and 1170 nm (Fig. 4C, I). The ground-state bleach showed multiple negative bands at 610 nm, 670 nm and 755 nm, and the stimulated emission produced a negative band at 900 nm (blue arrow in Fig. 4I). The decay curves of these bands are rather similar to those of HCy1 (Fig. S16) or HHCy1 (Fig. S17). When benzoindolium is introduced to the cyanine moiety of VIPI-4 or VIPI-5, the excited-state absorption bands move to about 490, 580, 700 and 1280 nm, accompanied by redshifts of ground-state bleach bands above 750 nm (Fig.s S20 and S21). These variations indicate that excitation of VIPIs depends on the cyanine moiety as LE, in agreement with the above steady state absorption spectra and molecular calculations. Interestingly, the NIR-II absorption signals (at about 1060 nm for VIPI-1/2/3; at 1280 nm for VIPI-4/5) decay from positive to slightly negative, implying two distinct processes, which are speculated to be from the LE to ICT state (Fig. 4D). However, in general, the LE state is the dominating excited state in chloroform.

In DMSO (Fig. 4E, F), the ICT state in VIPIs can be observed more distinctly, except VIPI-3. Upon excitation, the excited-state absorption band of VIPI-2 appears at 463 nm and decay rapidly, accompanied by the delayed appearance of a new peak at about 433 nm (Fig. 4G, J). The ground-state bleach band at 740 nm undergoes a process of rapid decrease, followed by an increase and then a slow decay, indicating inter-states transformation (Fig. 4H). In NIR-II windows, the negative stimulated emission band at 900 nm is generated within the initial 1 ps (Fig. 4H), similar to that observed in chloroform (assigned as LE); it then rapidly decays and reverses to produce a positive absorption (blue arrow in Fig. 4J). Meanwhile, a gradually redshifted negative stimulated emission band emerges above 1000 nm due to the solvent relaxation (red arrow in Fig. 4J), which is a signature of the ICT state[47]. These features, including signal inversions and redshifts, are noticeably observed for VIPI-1 (Fig. S18), VIPI-4 (Fig. S20) and VIPI-5 (Fig. S21) in DMSO. However, VIPI-3 shows no apparent inter-states transformation in DMSO (Fig. S19), suggesting the sole presence of LE state without ICT state, which explains the blue-shift and small Stokes shift in the steady state spectra.

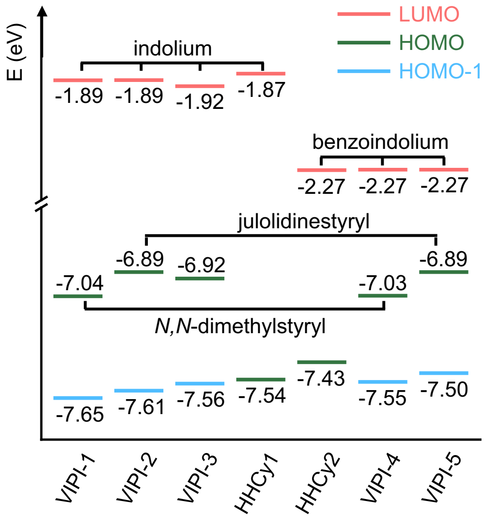

Fig. 2 | Energy level diagram of frontier molecular orbitals of VIPIs and HHCys. For HHCy1 and HHCy2, their HOMO is close to the HOMO-1 of VIPIs. Unit: eV.

Combining the results of femtosecond transient absorption spectra and TD-DFT calculation, comprehensive excitation and emission processes can be depicted in Fig. 4K. During the excitation process, the cyanine moiety is locally excited (HOMO-1 → LUMO, LE). Subsequently, the charge transfer occurs from styryl (HOMO) to the excited cyanine (HOMO-1), resulting in a hole in the styryl moiety. Finally, the excited electron in the cyanine moiety returns to the HOMO of the styryl moiety, emitting ICT fluorescence. The different features during the two processes are responsible for the unusually large Stokes shifts. Moreover, it can be concluded that the styryl moiety (donor) has a more significant influence on the emission wavelength, but the cyanine moiety regulates mainly the absorption wavelength.

In Vivo multicolor imaging

In phosphate buffered saline (PBS), VIPIs exhibited weak fluorescence (Fig. S1). However, in PBS containing 10% fetal bovine serum (10% FBS), these fluorophores displayed significant fluorescence, presumably due to their unspecific interaction[48]. VIPIs demonstrated not only excellent stability in PBS, 10% FBS and albumin solutions (Fig. S22), but also good photostability under the excitation of 808 nm laser (Fig. S23). Furthermore, VIPIs showed relatively high brightness at physiological pH (Fig. S24), suggesting that they may be suitable for biological imaging.

Then, VIPIs were imaged in 10% FBS under 730 nm (18.6 mW/cm^2) and 808 nm excitation (100 mW/cm^2) with the 1000 nm LP filter (Fig. S25). Under 730 nm excitation, VIPI-1 and VIPI-2 showed bright NIR-II fluorescence due to their matched absorption and higher quantum yield. Under the 808 nm excitation, VIPI-2 and VIPI-4 displayed intense NIR-II fluorescence, while VIPI-5 showed relatively weak fluorescence. This highlights the versatility of VIPI-2 under different excitations. Furthermore, VIPI-1 and VIPI-4 demonstrated minimal fluorescence cross-talk in different channels (Fig. S25), suggesting their potential in multicolor imaging.

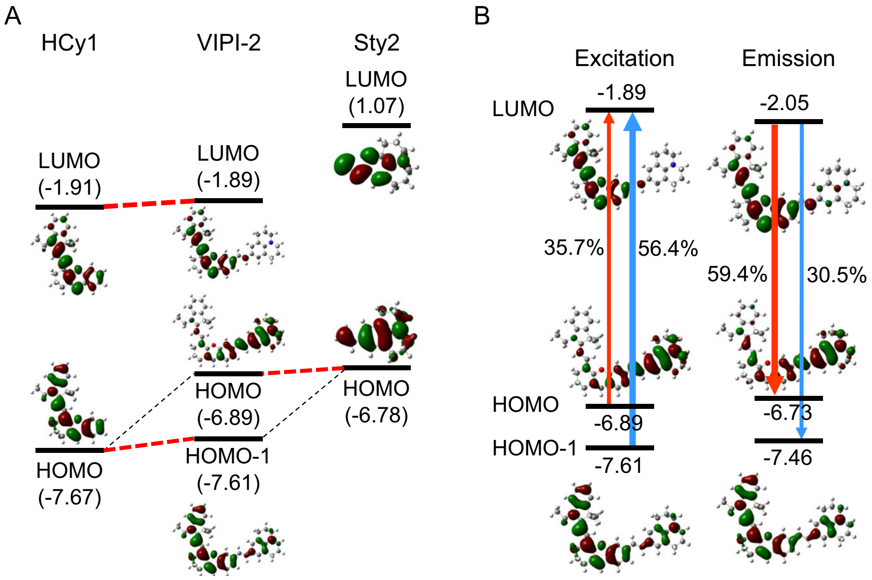

Fig. 3 | The large Stokes shifts of VIPI-2 explained by molecular orbital energy and excitation-emission process. A Energy level diagram of VIPI-2 and its substructures. Red dotted lines represent the strong coupling between the two molecular orbitals; black dotted lines indicate the weak coupling between the two molecular orbitals. The energy levels are annotated in parentheses (unit: eV). **B** Illustration of the excitation and emission processes between S_0 and S_1 of VIPI-2. The molecular orbitals and energy levels (unit: eV) of VIPI-2 in S_0 and S_1 are shown nearby. Red and blue arrows represent the ICT and LE characters, respectively; the percentages of the transition contributions of molecular orbitals are also noted.

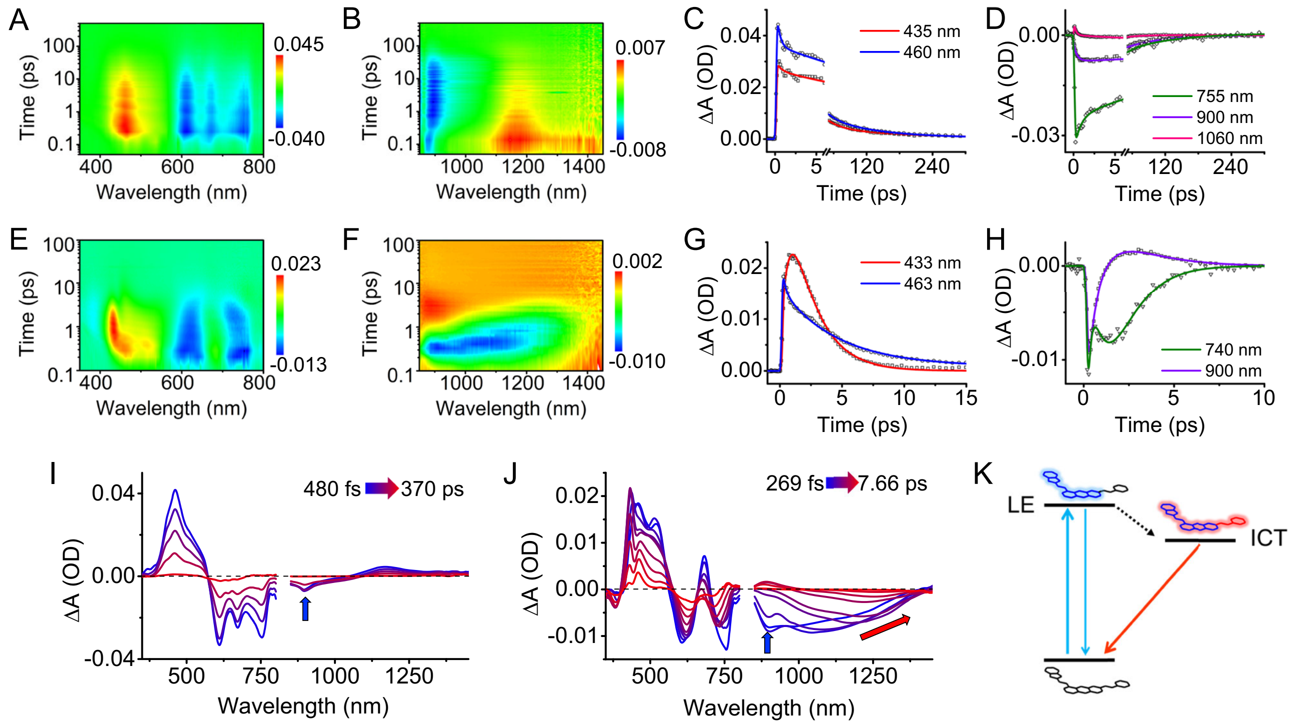

Fig. 4 | The large Stokes shifts of VIPI-2 explained by femtosecond transient absorption spectra. Femtosecond transient absorption spectra of VIPI-2 in chloroform (**A** and **B**) and DMSO (**E** and **F**). Kinetic profiles of VIPI-2 at selected wavelengths in chloroform (**C** and **D**) and DMSO (**G** and **H**). Time-evolution absorption spectra of VIPI-2 in chloroform (**I**) and DMSO (**J**). The horizontal dotted line denotes the base line. **K** Schematic diagram of the photophysical process of VIPI-2.

Multicolor imaging in NIR-II window can visualize multiple deep-seated structures simultaneously, which benefits a more comprehensive understanding of spatial relationships and interactions in vivo[49,50]. As shown in Fig. 5A, three isolated channels can be established with VIPI-1 (excitation: 730 nm; filter: 1000 nm LP), VIPI-4 (excitation: 808 nm; filter: 1000 nm LP) and VIX-4 (excitation: 980 nm; filter: 1150 nm LP). To demonstrate their applicability in in vivo imaging, VIPI-1, VIPI-4, and VIX-4 were separately administrated via gavage, clyster, and intravenous injection. Then, the stomach, intestine, and blood vessels of mice were imaged under different channels. After merging the three channels, a distinct image of the stomach and intestines in mice was obtained (Fig. 5B), along with clear visualization of the vascular structure throughout the entire body. Therefore, the combination of VIPI-1, VIPI-4, and VIX-4 provides an effective multicolor NIR-II imaging tool that can display multiple organs simultaneously.

Metabolism of PEGylated dye

Conjugatable NIR-II fluorophore is essential for labeling various biomacromolecules[51,52]. Polyethylene glycol (PEG) is commonly used as pharmaceutical excipient to improve the solubility and pharmacokinetics of drugs in vivo[53]. Therefore, we have developed a further conjugatable derivative of VIPI-2, VIPI-2-COOH (Fig. 6A), and demonstrated its application to investigating the metabolism of PEGylated dye in vivo.

To make VIPI-2 conjugatable, hexanoic acid was introduced to its indole moiety. The resulting VIPI-2-COOH displayed similar spectroscopic properties to VIPI-2 (Fig. S26 and Table S4). Then, NH_2-mPEG$_{2000}$ (see Supplementary Information) was conjugated to VIPI-2-COOH, yielding VIPI-2-mPEG$_{2000}$ conjugate, which exhibited slightly shifted absorption and fluorescence (Fig. S27). Notably, it showed improved solubility (the stock solution can be prepared in water without organic cosolvent) and significantly increased fluorescence (quantum yield ~ 0.09%) in PBS compared to VIPI-2; the fluorescence quantum yield of the conjugates can be further enhanced to 0.42% in 10% FBS (Fig. S28). In addition, VIPI-2-COOH can be also conjugated to other similar macromolecules, such as hydroxypropyl-β-cyclodextrin[54] (HPβCD, an important drug adjuvant), forming the corresponding conjugate VIPI-2-HPβCD (Figs. S29, S30, and S87).

Next, we administered VIPI-2 and VIPI-2-mPEG$_{2000}$ (both having no significant toxicity, Fig. S31) to mice intravenously and observed their distinctive metabolic behaviours. As shown in Fig. S32, after intravenous injection, VIPI-2 accumulates in the liver, with the intestine beginning to illuminate an hour later, indicating hepatobiliary excretion. After 24 h, the fluorescence intensity in liver declines dramatically, and the intestine no longer shows obvious fluorescence. According to Fig. S32, the half-life of VIPI-2 in mice is found to be about 21.7 h (Fig. 6B); VIPI-2-mPEG$_{2000}$ exhibits hepatobiliary metabolic pathway as well with clearer intestinal images and an increased half-life of 42.7 h (Fig. 6C). Moreover, approximately 17% of VIPI-2-mPEG$_{2000}$ was eliminated through urine in the first 8 h (Fig. 6D, Fig. S33). Hence, VIPI-2-mPEG$_{2000}$ shows a partial renal-clearance pathway compared with VIPI-2, indicating that the PEGylated dye with improved water-solubility can reduce nonspecific uptake by the reticuloendothelial system.

Bone imaging over 1300 nm

The substantial Stokes shifts of VIPIs effectively minimize the scattering of excitation light, and their pronounced residual fluorescence at longer wavelengths suggests great potential for long-wavelength imaging applications. Therefore, it may be anticipated that utilizing VIPIs in bioimaging could enhance imaging quality.

VIPI-4 was chosen as the representative fluorophore due to its relatively strong fluorescence under the excitation of 808 nm laser (Fig. S25). To improve water solubility, VIPI-4 was encapsulated in

DSPE-mPEG$_{2000}$ liposomes. As shown in Fig. 7A-B and Figu. S34, the liposomes exhibit remarkable NIR-II fluorescence in saline, with a hydrodynamic diameter of 13.8 ± 0.4 nm, dye content of about 7.9%, and a fluorescence quantum yield of 0.01% (in PBS). For in vivo imaging, VIPI-4 liposomes, with good biocompatibility (Fig. S31), were administered to mice via tail vein injection. Images were captured using 1000 nm, 1150 nm, and 1300 nm LP filters to evaluate the imaging quality at longer wavelengths (Fig. S35). The images from the 1300 nm LP filter provided clearer visualization of blood vessels, particularly allowing measurement of abdominal vessel diameters in mice (Fig. S35I), which was challenging in the other images (Fig. S35G and S35H). Besides, a comparative study with ICG dye (Fig. S36) also demonstrated that our probe with large Stokes shift can achieve a higher signal-to-background ratio (SBR) of 1.8 than ICG (SBR 1.5) when using 1300 nm LP filter, though a comparative SBR of 1.3 versus 1.2 was observed when using the 1150 nm LP filter. This clearly indicates that VIPI-4 liposomes with large Stokes shift can achieve better image quality.

The time lapse imaging revealed the fluorescence in mouse liver and spleen gradually increases, indicating that VIPI-4 liposomes firstly enter the liver and spleen. After 1 h, the fluorescence declines with a half-life of 5.3 h (Fig. S37). However, after 24 h, significant fluorescence also appears in bones, as evidenced by the distinct visualization of the mouse spine from a ventral view (Fig. 7C), suggesting a gradual accumulation of VIPI-4 liposomes in bones. Recent studies on bone-targeting probes showed that macrophages in the bone marrow may play a role, though the exact underlying mechanisms may be varied and complex[55–58]. For VIPI-4 liposomes, their accumulation in bones might be attributed to that marrow macrophages transported the nanosized VIPI-4 liposomes with a size of about 14 nm (Fig. S34) to bone marrow, because small nanoparticles (about ~15 nm)[56] was found to be favorable for bone marrow retention. In other words, the possible bone-targeting mechanism of VIPI-4 liposomes might result from their effective interaction with marrow macrophages (including their favorable size). Comparisons of images captured through 1000, 1150, and 1300 nm LP filters showed that as the cut-off wavelength increased, the clarity and signal-to-background ratio of the spine structure improved both in vivo and in skinned imaging (Fig. 7C, D).

Taking the advantage of the bone-targeting ability of VIPI-4 liposomes, we then focused on imaging the knee joints of mice. Images of the knee joints were captured with different LP filters 24 h post-injection. As shown in Fig. 7E, compared to the 1000 LP image, the gap between the tibia and the medial condyle of the tibia can only be observed in 1150 and 1300 LP images; moreover, the patella is only visible in the 1300 LP images. The fine structure of knee joint, captured in vivo with 1300 nm LP, demonstrates the overall superiority of VIPI-4 with relatively large Stokes shift and high brightness. The detailed bone structures were also validated by fluorescence imaging of mouse knee joint after muscle stripping (Fig. 7E4-E6). The above results suggest that VIPI-4 may serve as a superior fluorescent bone imaging reagent, and displays potential for in vivo monitoring of bone diseases, such as fracture and osteoarthritis[28,55–58].

In summary, we have proposed VIPIs as NIR-II fluorophores, which are characterized by a highly asymmetric framework with *p*-aminostyryl as the electronic donor and hemicyanine as the electronic acceptor. These fluorophores (except for VIPI-3) exhibit NIR-II fluorescence and large Stokes shifts (167–260 nm). Mechanisms studies by femtosecond transient absorption spectroscopy and TD-DFT disclose that the excitation process is predominantly localized within the cyanine moiety, whereas the emission involves significant ICT from the cyanine to styryl moiety, by which we can regulate the absorption and emission wavelengths separately. Using VIPI-1 and VIPI-4, we achieved multicolor NIR-II imaging in mice, enabling simultaneous visualization of the stomach, intestine, and vessels in vivo. Furthermore, the development of conjugatable VIPI-2-COOH allowed the imaging of metabolic pathways of PEGylated dyes. Finally, VIPI-4 facilitated imaging of the fine structures of knee joint in mice at wavelengths over 1300 nm, showcasing the advantage of its large Stokes shift. This study suggests that simultaneously adjusting LE and ICT components in the donor-acceptor framework may be a promising strategy for designing new fluorophores with long emission and large Stokes shifts.

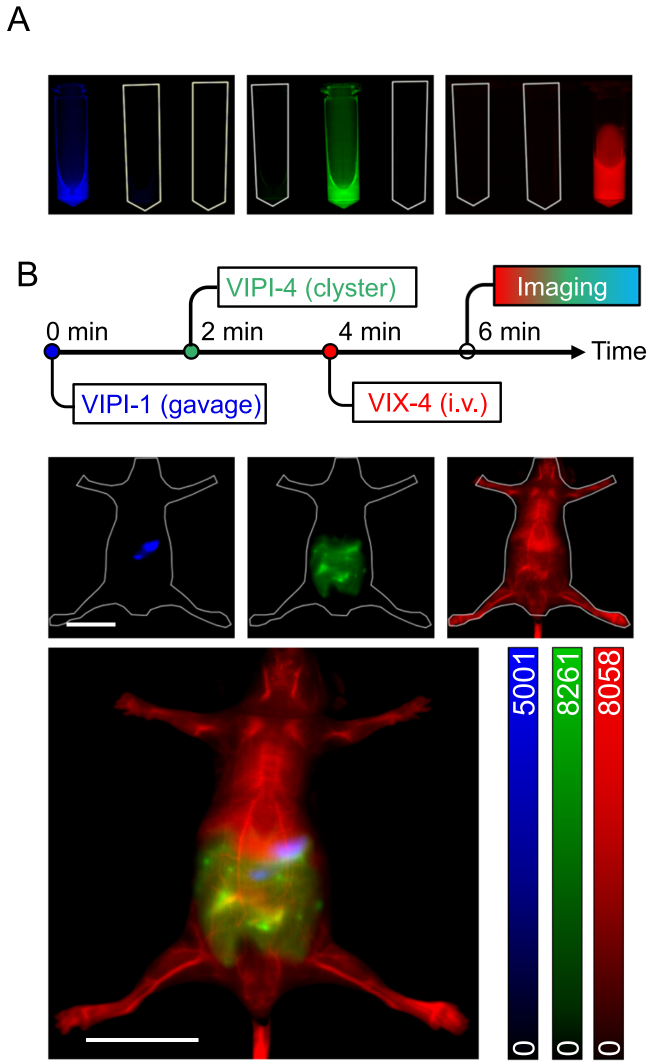

Fig. 5 | Multicolor imaging by VIPIs. A The multicolor imaging of three vials containing VIPI-1 (left, 10 μM in 10% FBS), VIPI-4 (middle, 10 μM in 10% FBS), and VIX-4 (right, 0.2 mg/mL liposomes in water) under different excitations. Blue channel: 730 nm excitation, 1000 nm LP, exposure time (ET) = 50 ms; green channel: 808 nm excitation, 1000 nm LP, ET = 30 ms; red channel: 980 nm excitation, 1150 nm LP, ET = 100 ms. **B** Dosing scheme for multicolor imaging experiment and representative in vivo multicolor imaging of mice ($n = 3$ mice). VIPI-1 (500 μM, 100 μL), VIPI-4 (500 μM, 200 μL), and VIX-4 (10 mg/mL, 200 μL) were separately administrated via gavage, clyster, and intravenous injection (i.v.). Dosing scheme (the first row); three single color channels (the second row); the merged three-color channel (the bottom). Blue channel: ET = 100 ms; green channel: ET = 100 ms; red channel: ET = 200 ms. Scale bars, 1 cm.

Methods

Ethical statement

All animal care and experimental protocols complied with the Animal Management Rules of the Ministry of Health of the People's Republic of China and were approved by the Institute of Process Engineering, Chinese Academy of Science (protocol number: IPEAECA2022071).

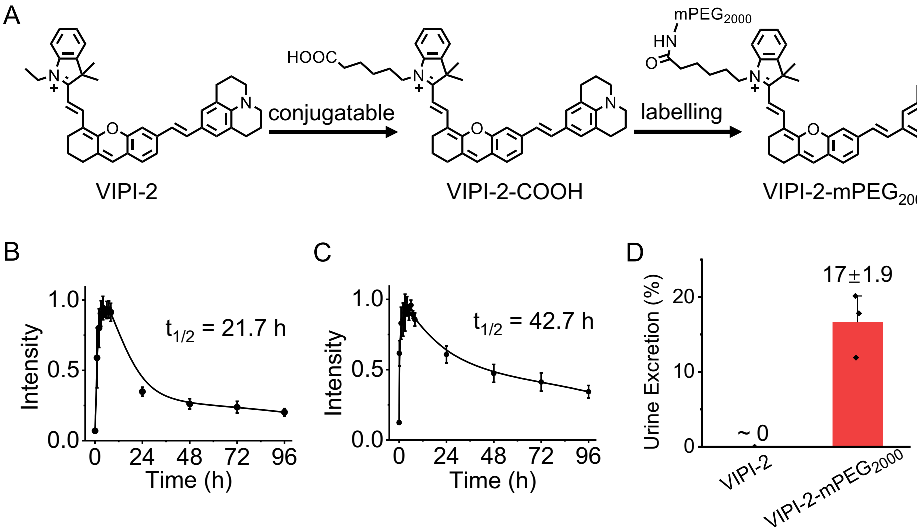

Fig. 6 | Synthesis and characterization of PEGylated Dye. A Conjugatable design of VIPI-2-COOH. The pharmacokinetics of (**B**) VIPI-2 and (**C**) VIPI-2-mPEG$_{2000}$ in mice after tail vein injection (VIPI-2: 500 μM, 200 μL in saline containing 1% DMSO; VIPI-2-mPEG$_{2000}$: 500 μM, 200 μL in saline) determined by NIR-II imaging. **D**The fractions of urine excretion of VIPI-2 and VIPI-2-mPEG$_{2000}$ within 8 h after intravenous injection. Data are presented as mean ± standard deviation; $n = 3$ mice for panels **B**, **C** and **D**.

Syntheses and general methods

For all syntheses, characterization and additional details, please see Supplementary Information.

Spectroscopic measurements

The stock solutions of VIPI-1 to VIPI-5 and ICG (50 mM) were prepared with DMSO. The stock solution of VIPI-2-mPEG$_{2000}$ (500 μM) and VIPI-4 liposome (20 mg/mL) were prepared in physiological saline. All the fluorophores were diluted to 10 μM with the corresponding solvent to measure the absorption or fluorescence spectra, unless otherwise noted.

Measuring the photophysical data

The molar absorption coefficient (ε) value was calculated by measuring the absorbance of serial diluted solutions.

The fluorescence quantum yield (Φ) was measured via the following equation:

$$\Phi_X = \Phi_S \frac{R_X}{R_S}\left(\frac{\eta_X}{\eta_S}\right)^2$$

where the subscripts S and X mean the standard and test sample, respectively; R is the slope from the integrated emission intensity versus absorbance. η is the refractive index of solvents. All the dyes were measured by using ICG (Φ = 0.9 % in water) as a standard[59]; HHCy1, HHCy2, VIPI-1, VIPI-2, VIPI-3, VIPI-2-COOH, VIPI-2-mPEG$_{2000}$ and ICG were excited at 660 nm; VIPI-4, VIPI-4 liposomes, VIPI-5 and ICG were excited at 808 nm. The absorbance of the above compounds kept below 0.05 at the excited wavelength.

DFT calculations

The ground state (S_0) of all structures was optimized at the ωB97XD/TZVP level. All solvent effects (in chloroform) were considered using a solvent model based on density. The TD-DFT calculation used the TD-ωB97XD/TZVP method to optimize the first excited states (S_1). All the calculation was performed using the Gaussian 16, Revision C.01.

Femtosecond transient absorption (TA) analysis

Ultrafast transient absorption spectroscopy was measured with a femtosecond Ti: sapphire laser system (Coherent) and Helios pump-probe system (Ultrafast Systems). The laser system, a Legend Elite-1K-HE regenerative amplifier (800 nm, 25 fs, 4 mJ/pulse, and 1 kHz repetition rate), was seeded with a mode-locked Ti: sapphire laser system (Vitara). The major output light was directed into the optical parametric amplifiers (TOPAS-C) to generate pump pulses with tunable wavelengths (300 nm to 2.5 μm). These pump pulses were modulated at 500 Hz using a synchronized optical chopper, allowing alternate acquisition of TA spectra with and without excitation. Pump intensity was finely adjusted using a variable neutral density filter. A small part of the amplifier output light was sent through a motorized optical delay line and subsequently focused onto a sapphire crystal to produce a white-light continuum (WLC) ranging from 350–800 nm, or 850–1450 nm. The WLC light was focused onto the sample and then introduced into a fiber-coupled spectrometer for measurement at 1 KHz. To compensate for pulse-to-pulse fluctuations, a reference beam was split from the WLC. Time delays between the pump and probe pulses were precisely controlled by adjusting the optical path via the motorized delay line. All measurements were carried out under ambient conditions.

Animal handling

8-Week-old female BALB/c nude mice were obtained from Beijing Vital River Laboratory Animal Technology Co., Ltd. Mice were housed under controlled temperature at 20–25 °C and 12 h light/dark cycle, along with sterilized food and purified water. Before imaging, the mice were anaesthetized using air mixing with 4% isoflurane. Mice were randomly selected from cages for all experiments.

Biosafety assessment

The in vivo toxicity was evaluated by hematoxylin and eosin (H&E) staining of mouse tissues. The mice were randomly divided into 4 groups: control group, VIPI-2 group, VIPI-2-mPEG$_{2000}$ group and VIPI-4 liposome group. Each group contained 3 mice. The mice were intravenously injected with 200 μL solution of saline, VIPI-2 (500 μM), VIPI-2-mPEG$_{2000}$ (500 μM) and VIPI-4 liposomes (20 mg/mL), respectively. The mice were fed for 7 days

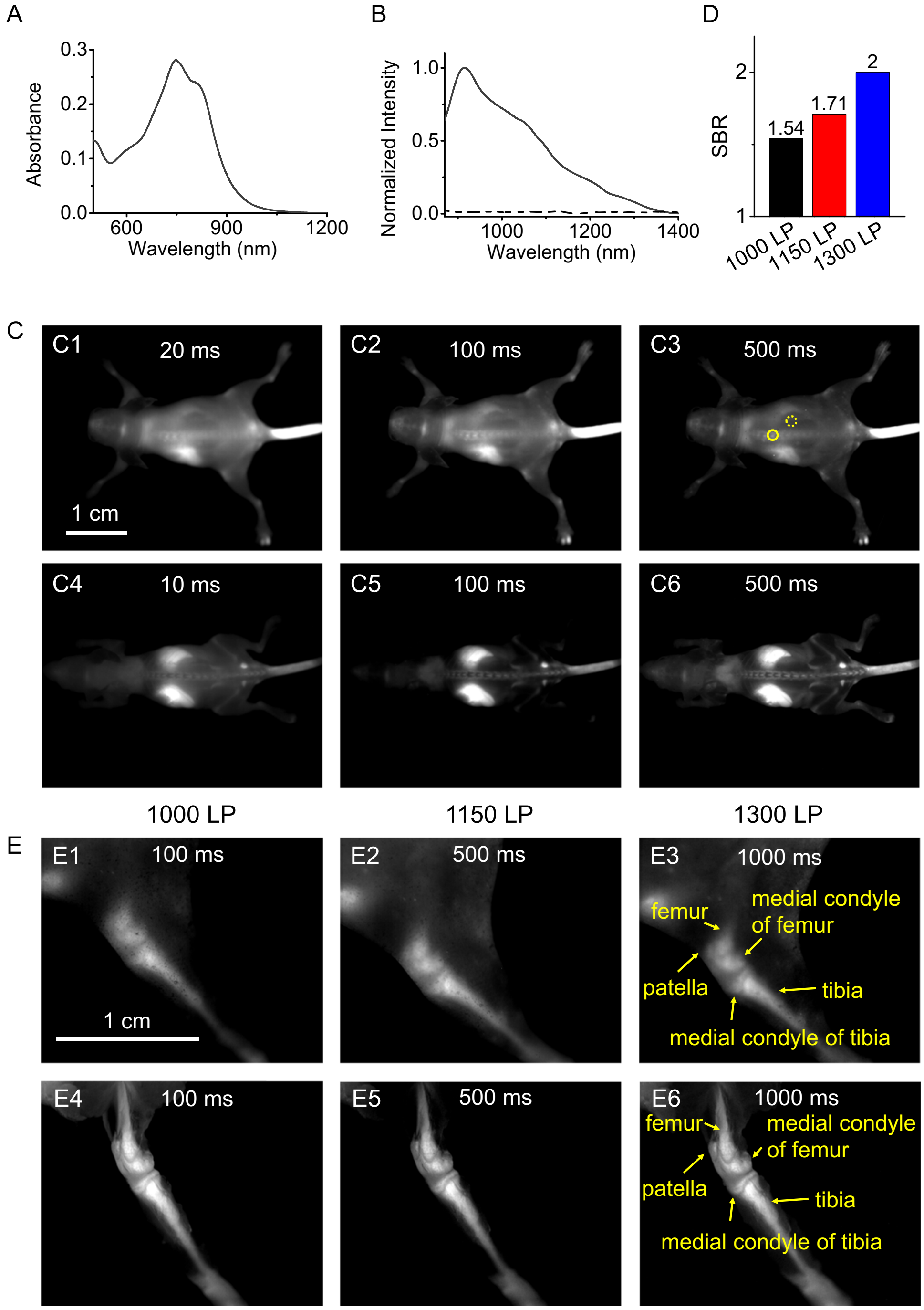

Fig. 7 | Spectral properties of VIPI-4 liposomes and fluorescence imaging of mouse bones under different LP filters. The absorption (**A**) and normalized fluorescence (**B**) spectra of VIPI-4 liposomes (0.2 mg/mL) in saline. The normalized fluorescence of VIPI-4 (10 μM, dash line) was shown for reference. **C** The bone imaging of (C1-C3) in vivo and (C4-C6) skinned mice from ventral view after 24 h intravenous injection of VIPI-4 liposomes (20 mg/mL, 200 μL). The exposure time is shown in each image. **D** The SBR of images C1-C3. SBR is the fluorescence intensity ratio in the yellow solid line circle (spine area) and dashed line circle (non-bone area) with the same area (for clarity, these positions are indicated in image C3 only). The SBR values are noted on the column. **E** Representative images of knee joints of mice (*n* = 3 mice). (E1-E3) In vivo fluorescence images of knee joints of mice. (E4-E6) Fluorescence images of knee joints of mice after stripping muscle. The skeleton names are marked in images E3 and E6.

under normal conditions, and then were euthanized. The major organs (heart, liver, spleen, lung and kidney) were harvested and immediately frozen in liquid nitrogen. Next, frozen sections of 10 μm were made on a cryostat microtome (CM3050S, Leica). Then, the sections were treated with cool methanol and subjected to standard H&E staining. The H&E images were recorded with a microscope (IX83, Olympus) with color camera (FL20, Tucsen).

In vivo NIR-II imaging

Fluorescence imaging was carried out on In-vivo Master (Grand-imaging Technology) equipped with an InGaAs camera C-RED2 (Firstlight). Mice were anaesthetized and placed on a stage for injection. In multicolor imaging, the solutions of VIPI-1 and VIPI-4 were freshly prepared at 500 μM in sterile saline containing 1% DMSO as cosolvent and administrated at a dose of 200 μL via gavage and clyster sequentially. Next, the VIX-4 liposomes were administrated via the tail vein injection. Then the mice were set on the platform for imaging. VIPI-1 was excited with 730 nm laser (18.6 mW/cm^2) and 1000 nm LP filter (Edmund Optics); VIPI-4 was excited with 808 nm laser (100 mW/cm^2) and 1000 nm LP filter; VIX-4 was excited with 980 nm laser (100 mW/cm^2) and 1150 nm LP filter (Edmund Optics).

In metabolic imaging, the injection solution was freshly prepared by adding 2 µL stock solution of VIPI-2 (50 mM in DMSO) into 198 µL sterile saline to a final concentration of 500 µM. The VIPI-2-mPEG$_{2000}$ injection solution was prepared by directly dissolving VIPI-2-mPEG$_{2000}$ powder in sterile saline to 500 µM. Then, 200 µL of each solution was injected via the tail vein of mice, followed by time-lapse imaging at various time points. At the same time, mouse urine samples were collected. Imaging was performed with 808 nm laser (50 mW/cm^2) and 1000 nm LP filter (Edmund Optics).

In imaging with VIPI-4 liposomes, lyophilized VIPI-4 liposomes were directly dissolved in sterile saline to obtain injection solution (20 mg/mL). Then, 200 µL of the solution was injected into mice via tail vein. After 24 h, mice were placed on the platform for the bone imaging through skin firstly. Then, the skin or muscle of the mice were stripped, and the mice were imaged again for comparison. VIPI-4 liposomes were excited by 808 nm laser (100 mW/cm^2) and captured though 1000/1150/1300 nm LP filters.

Reporting summary

Further information on research design is available in the Nature Portfolio Reporting Summary linked to this article.

Data availability

The data generated in this study are provided in Source Data file. The full image dataset is available from the corresponding author upon request. Source data are provided with this paper.

References

1. Li, X. et al. Design strategies for water-soluble small molecular chromogenic and fluorogenic probes. *Chem. Rev.* **114**, 590–659 (2014).
2. Li, H. et al. Activity-based NIR fluorescent probes based on the versatile hemicyanine scaffold: design strategy, biomedical applications, and outlook. *Chem. Soc. Rev.* **51**, 1795–1835 (2022).
3. Yan, K. et al. Ultra-photostable small-molecule dyes facilitate near-infrared biophotonics. *Nat. Commun.* **15**, 2593 (2024).
4. He, S. et al. Crucial breakthrough of second near-infrared biological window fluorophores: design and synthesis toward multimodal imaging and theranostics. *Chem. Soc. Rev.* **47**, 4258–4278 (2018).
5. Wu, Q. et al. Multivalent supramolecular fluorescent probes for accurate disease imaging. *Sci. Adv.* **10**, eadp8719 (2024).
6. Yang, Q. et al. Rational design of high brightness NIR-II organic dyes with S-D-A-D-S structure. *Acc. Chem. Res.* **2**, 170–183 (2021).
7. Lei, Z. et al. Molecular engineering of NIR-II fluorophores for improved biomedical detection. *Angew. Chem. Int. Ed.* **60**, 16294–16308 (2021).
8. Zhang, W. et al. Photoactivation inducing multifunctional coupling of fluorophore for efficient tumor therapy in situ. *Adv. Mater.* **36**, 2314021 (2024).
9. Zhou, H. et al. Upconversion NIR-II fluorophores for mitochondria-targeted cancer imaging and photothermal therapy. *Nat. Commun.* **11**, 6183 (2020).
10. Liu, Z. et al. Breaking through the size control dilemma of silver chalcogenide quantum dots via trialkylphosphine-induced ripening: leading to Ag_2Te emitting from 950 to 2100 nm. *J. Am. Chem. Soc.* **143**, 12867–12877 (2021).
11. Xu, W. et al. NIR-II AIEgens: a win-win integration towards bioapplications. *Angew. Chem. Int. Ed.* **60**, 7476–7487 (2021).
12. Zhang, X. et al. Dihydropyridopyrazine functionalized xanthene: generating stable NIR dyes with small-molecular weight by enhanced charge separation. *Angew. Chem. Int. Ed.* **63**, e202410666 (2024).
13. Liu, J. et al. Precision navigation of hepatic ischemia–reperfusion injury guided by lysosomal viscosity-activatable NIR-II fluorescence. *J. Am. Chem. Soc.* **144**, 13586–13599 (2022).
14. Bian, H. et al. Cardiolipin-targeted NIR-II fluorophore causes "avalanche effects" for re-engaging cancer apoptosis and inhibiting metastasis. *J. Am. Chem. Soc.* **144**, 22562–22573 (2022).
15. Tian, R. et al. Albumin-chaperoned cyanine dye yields superbright NIR-II fluorophore with enhanced pharmacokinetics. *Sci. Adv.* **5**, eaaw0672 (2019).
16. Cosco, E. et al. Shortwave infrared polymethine fluorophores matched to excitation lasers enable non-invasive, multicolour in vivo imaging in real time. *Nat. Chem.* **12**, 1123–1130 (2020).
17. Li, Z. et al. In situ orderly self-assembly strategy affording NIR-II-J-aggregates for in vivo imaging and surgical navigation. *Nat. Commun.* **14**, 1843 (2023).
18. Lu, L. et al. NIR-II bioluminescence for in vivo high contrast imaging and in situ ATP-mediated metastases tracing. *Nat. Commun.* **11**, 4192 (2020).
19. Ding, B. et al. Polymethine thiopyrylium fluorophores with absorption beyond 1000 nm for biological imaging in the second near-infrared subwindow. *J. Med. Chem.* **62**, 2049–2059 (2019).
20. Bandi, V. et al. Targeted multicolor in vivo imaging over 1000 nm enabled by nonamethine cyanines. *Nat. Methods* **19**, 353–358 (2022).
21. Qin, Z. et al. NIRII-HDs: A versatile platform for developing activatable NIR-II fluorogenic probes for reliable in vivo analyte sensing. *Angew. Chem. Int. Ed.* **61**, e202201541 (2022).
22. Xu, W. et al. A peierls transition in long polymethine molecular wires: evolution of molecular geometry and single-molecule conductance. *J. Am. Chem. Soc.* **143**, 20472–20481 (2021).
23. Swamy, M. et al. Shortwave-infrared fluorescent molecular imaging probes based on π-conjugation extended indocyanine Green. *Bioconjug. Chem.* **32**, 1541–1547 (2021).
24. Yue, Y. et al. Biomedical-optical-window tailored cyanines for steerable inflammatory bowel disease theranostic. *Adv. Mater.* **36**, 2408450 (2024).
25. Li, B. et al. Organic NIR-II molecule with long blood half-life for in vivo dynamic vascular imaging. *Nat. Commun.* **11**, 3102 (2020).
26. Chen, H. et al. Bioinspired large Stokes shift small molecular dyes for biomedical fluorescence imaging. *Sci. Adv.* **8**, eabo3289 (2022).
27. Likhotkin, I. et al. Photoactivatable large Stokes shift fluorophores for multicolor nanoscopy. *J. Am. Chem. Soc.* **145**, 1530–1534 (2023).
28. Pan, H. et al. Rational design of asymmetric polymethines to attain NIR(II) bioimaging at >1100 nm. *J. Am. Chem. Soc.* **145**, 516–526 (2023).
29. He, L. et al. Engineering of reversible NIR-II redox-responsive fluorescent probes for imaging of inflammation in vivo. *Angew. Chem. Int. Ed.* **61**, e202211409 (2022).
30. Dou, K. et al. Design of activatable NIR-II molecular probe for in vivo elucidation of disease-related viscosity variations. *Anal. Chem.* **92**, 4177–4181 (2020).
31. Santos, E. et al. Design of large Stokes shift fluorescent proteins based on excited state proton transfer of an engineered photobase. *J. Am. Chem. Soc.* **143**, 15091–15102 (2021).
32. Ren, T. et al. A general method to increase Stokes shift by introducing alternating vibronic structures. *J. Am. Chem. Soc.* **140**, 7716–7722 (2018).
33. Peng, X. et al. Heptamethine cyanine dyes with a large stokes shift and strong fluorescence: a paradigm for excited-state intramolecular charge transfer. *J. Am. Chem. Soc.* **127**, 4170–4171 (2005).

34. Yang, J. et al. Organic fluorophores with large Stokes shift for the visualization of rapid protein and nucleic acid assays. *Angew. Chem. Int. Ed.* **63**, e202318800 (2024).
35. Mieczkowski, M. et al. Large Stokes shift fluorescence activation in an RNA aptamer by intermolecular proton transfer to guanine. *Nat. Commun.* **12**, 3549 (2021).
36. Huang, K. et al. Structural basis of a small monomeric Clivia fluorogenic RNA with a large Stokes shift. *Nat. Chem. Biol.* **20**, 1453–1460 (2024).
37. Li, J. et al. Stable, bright, and long-fluorescence-lifetime dyes for deep-near-infrared bioimaging. *J. Am. Chem. Soc.* **144**, 14351–14362 (2022).
38. Liu, D. et al. Xanthene-based NIR-II dyes for in vivo dynamic imaging of blood circulation. *J. Am. Chem. Soc.* **143**, 17136–17143 (2021).
39. Zeng, Z., Liew, S. S., Wei, X. & Pu, K. Y. Hemicyanine-based near-infrared activatable probes for imaging and diagnosis of diseases. *Angew. Chem. Int. Ed.* **60**, 26454–26475 (2021).
40. Li, B. et al. An efficient 1064 nm NIR-II excitation fluorescent molecular dye for deep-tissue high-resolution dynamic bioimaging. *Angew. Chem. Int. Ed.* **57**, 7483–7487 (2018).
41. Dou, K. et al. Flexible designing strategy to construct activatable NIR-II fluorescent probes with emission maxima beyond 1200 nm. *Anal. Chem.* **93**, 4006–4014 (2021).
42. Thimsen, E., Sadtler, B. & Berezin, M. Y. Shortwave-infrared (SWIR) emitters for biological imaging: a review of challenges and opportunities. *Nanophotonics* **6**, 1043–1054 (2017).
43. Chen, Q. et al. Safety and efficacy of indocyanine green tracer-guided lymph node dissection during laparoscopic radical gastrectomy in patients with gastric cancer A randomized clinical trial. *JAMA Surg.* **155**, 300–311 (2020).
44. Hu, Z. et al. First-in-human liver-tumour surgery guided by multispectral fluorescence imaging in the visible and near-infrared-I/II windows. *Nat. Biomed. Eng.* **4**, 259–271 (2020).
45. Zhu, S. et al. Near-Infrared-II (NIR-II) bioimaging via off-peak NIR-I fluorescence emission. *Theranostics* **8**, 4141–4151 (2018).
46. Zhang, W. et al. Solvation-dependent excited-state dynamics of donor–acceptor molecules with hybridized local and charge transfer character. *J. Phys. Chem. C.* **124**, 5574–5582 (2020).
47. Carlotti, B. et al. Photoinduced symmetry-breaking intramolecular charge transfer in a quadrupolar pyridinium derivative. *Phys. Chem. Chem. Phys.* **16**, 13984–13994 (2014).
48. Shang, J. et al. An oxazine-based fluorogenic probe with changeable π-conjugation to eliminate false-positive interference of albumin and its application to sensing aminopeptidase N. *Angew. Chem. Int. Ed.* **61**, e202205043 (2022).
49. Cosco, E. et al. Bright chromenylium polymethine dyes enable fast, four-color in vivo imaging with shortwave infrared detection. *J. Am. Chem. Soc.* **143**, 6836–6846 (2021).
50. Xu, J. et al. Biomimetic NIR-II fluorescent proteins created from chemogenic protein-seeking dyes for multicolor deep-tissue bioimaging. *Nat. Commun.* **15**, 2845 (2024).
51. Antaris, A. et al. A small-molecule dye for NIR-II imaging. *Nat. Mater.* **15**, 235–242 (2016).
52. Li, D. et al. Doubly strapped zwitterionic NIR-I and NIR-II heptamethine cyanine dyes for bioconjugation and fluorescence imaging. *Angew. Chem. Int. Ed.* **135**, e202305062 (2023).
53. D'souza, A. et al. Polyethylene glycol (PEG): a versatile polymer for pharmaceutical applications. *Expert Opin. Drug Discov.* **13**, 1257–1275 (2016).
54. Huang, J. et al. Renal-clearable molecular semiconductor for second near-infrared fluorescence imaging of kidney dysfunction. *Angew. Chem. Int. Ed.* **58**, 15120–15127 (2019).
55. Mi, C. et al. Bone disease imaging through the near-infrared-II window. *Nat. Commun.* **14**, 6287 (2023).
56. Chen, D. et al. NIR-II fluorescence imaging reveals bone marrow retention of small polymer nanoparticles. *Nano Lett.* **21**, 798–805 (2021).
57. Jia, S. et al. Water-soluble chromenylium dyes for shortwave infrared imaging in mice. *Chem* **9**, 3648–3665 (2023).
58. Zhang, P. et al. Carboxyl-modified quantum dots for NIR-IIb bone marrow imaging. *ACS Appl. Mater. Interfaces* **16**, 8509–8517 (2024).
59. Carr, J. A. et al. Shortwave infrared fluorescence imaging with the clinically approved near-infrared dye indocyanine green. *Proc. Natl. Acad. Sci. USA* **115**, 4465–4470 (2018).

Acknowledgements

We thank the financial support from the NSF of China (22174148, 22474147, 22374153, 22174147 and 22474144), Beijing Natural Science Foundation of China (2222044).

Author contributions

D.L. conceived the project and designed the study. D.L. performed the experiments. Z.H., W. G., J.S., Y.Y., and X.Z. carried out partial experiments. D.L. analyzed data and wrote the original manuscript. X.L. provided constructive suggestions for results and discussion. W.S. and H.M. revised the manuscript. W.S. supervised the overall study.

Competing interests

The authors declare no competing interests.

Additional information

Supplementary information The online version contains supplementary material available at https://doi.org/10.1038/s41467-025-60241-2.

Correspondence and requests for materials should be addressed to Wen Shi.

Peer review information *Nature Communications* thanks Dayong Jin, Tian-Bing Ren and the other, anonymous, reviewer(s) for their contribution to the peer review of this work. A peer review file is available.